Field-free Josephson diode effect in NbSe₂ van der Waals junction

Check for updates

Jiaxiang Ma [1], Huiyu Wang[2], Weizhuang Zhuo[2], Bin Lei[3], Shuai Wang[3], Wenxiang Wang[2], Xin-Yu Chen[1], Zhen-Yu Wang[2], Binghui Ge [3], Zhen Wang[2], Jing Tao[2], Kun Jiang [4], Ziji Xiang [1,5] ✉ & Xian-Hui Chen [1,2,5] ✉

Nonreciprocal transport is one of the cornerstones of modern electronics industry with semiconductor diode serving as the most celebrated representative. Recently, superconducting diode has been put forward to achieve nonreciprocal transport in the non-dissipative regime. However, most of superconducting diodes require the application of magnetic field, limiting their practical application. Here we report a field-free diode effect in the van der Waals Josephson junctions composed of 2H-NbSe₂ thin flakes without extra barrier layers. The unexpected large asymmetric current-voltage profile at zero field is observed in both overdamped and underdamped Josephson junctions. Under magnetic fields, the asymmetry of critical current is suppressed with a sign reversal. The realization of field-free Josephson diode with high rectification ratio in such a simple configuration not only implies an implicit spontaneous time-reversal symmetry breaking effect that challenges the existing theories, but also provides a promising avenue for the development of superconducting electronics and quantum devices.

As one of the most important semiconductor devices, diodes are widely used in the modern electronics industry, yet several limitations, such as heat generation, power consumption, and limited operating frequency put obstacles in their further developments. The recently emerged super-conducting diode can address these problems to some extent, owing to their evident advantages of low energy consumption and ultrahigh frequency[1,2]. The so-called superconducting diode effect (SDE) describes an intriguing nonreciprocity of critical supercurrents: the device acts as a superconductor for currents along one direction, but as a resistive metal for the opposite direction of current flow[3]. Up to date, SDE has been observed in various superconducting systems, such as artificial superlattices[4–6], thin flakes of two-dimensional materials[7], and Josephson junctions (JJs)[8–15]. Unfortunately, the SDE can only be manifested in superconducting systems with spontaneous breaking of the inversion symmetry (IS) and the time-reversal symmetry (TRS)[3,16–20]; whereas the IS breaking is inherently achieved in noncentrosymmetric superconductors or artificially stacked JJs, the TRS breaking (TRSB) mostly requires the introduction of external magnetic fields (H), which seriously hinders the application of superconducting diodes for a device perspective.

A JJ is typically composed of two superconductors connected by an insulating barrier or a conducting/superconducting weak link[21]. In common cases, the critical currents in JJs are reciprocal (i.e., identical for opposite current directions) and are described by the Josephson relations[22]. SDE in JJ, known as the Josephson diode effect (JDE), requires explicit symmetry breakings as well. A JJ with broken IS still exhibits reciprocal critical current at $H = 0$ ($|I_{c+}(0)| = |I_{c-}(0)|$) as long as the TRS is inherently preserved; in such case, nonreciprocity is expected at $H \neq 0$, i.e., $|I_{c+}(H)| \neq |I_{c-}(H)|(H \neq 0)$[3,11,16,17]. Therefore, the JDE occurs at zero magnetic field only if both IS and TRS are simultaneously broken[3]. In the absence of H, JDE can be invoked by insertion of magnetic barrier layer between the two super-conductors, which causes TRSB by providing a spin-splitting stray field[9]. An alternative approach to applicable zero-field JDE is to establish intrinsic TRSB in the superconducting state via manipulating the phases of order parameters between two superconductors; theoretically, this usually relies on the involvement of unconventional pairing symmetries[23,24] or multi-band superconductivity[25,26].

Layered dichalcogenide 2H-NbSe₂ is a van der Waals (vdW) crystal exhibiting robust superconductivity, thus naturally serves as a promising candidate for building highly transparent JJs by a simple stacking of thin flakes[27,28]. Field-induced SDE and field-free JDE have been reported in NbSe₂ few-layer flakes[7] and the NbSe₂/Nb₃Br₈/NbSe₂ heterostructures[11], respectively. In particular, the latter represents a rare example of realizing

[1]Hefei National Research Center for Physical Sciences at the Microscale, University of Science and Technology of China, Hefei, China. [2]Department of Physics, University of Science and Technology of China, Hefei, China. [3]Institutes of Physical Science and Information Technology, Anhui University, Hefei, China. [4]Beijing National Laboratory for Condensed Matter Physics and Institute of Physics, Chinese Academy of Sciences, Beijing, China. [5]Hefei National Laboratory, University of Science and Technology of China, Hefei, China. ✉e-mail: zijixiang@ustc.edu.cn; chenxh@ustc.edu.cn

zero-field JDE without introducing any magnetic components, despite that the exact origin of TRSB is still elusive. In this work, we report a field-free JDE in the basic vdW JJs composed of two NbSe$_2$ thin flakes (thickness ≈ 10 nm), which can exhibit abundant properties that are distinct from the bulk crystal or thick flakes, such as the orbital Fulde–Ferrell–Larkin–Ovchinnikov (FFLO) state and Ising pairing[29,30]. A sharp superconducting transition appears at 6.4–6.6 K proves the high quality of our devices. Surprisingly, an asymmetric current-voltage characteristic can be observed in the superconducting regime. The field-free JDE occurs in both underdamped and overdamped JJs, featured by stable and rapid superconducting half-wave rectification. Under external magnetic field, the nonreciprocal component of critical currents, ΔI_c ($|I_{c+}| - |I_{c-}|$), shows a sign reversal and displays symmetric field dependence. Our observations highlight an emergent TRSB effect in vdW JJs even without peculiar tunnel barriers, which calls for further theoretical understandings. Meanwhile, they provide opportunities for constructing practical superconducting electronic devices.

Results

Basic characteristics of NbSe$_2$ JJs

The 2H-NbSe$_2$ JJ devices were fabricated using a dry-transfer method in a top-down process[31], which can avoid interface contact with polymers. Fig. 1a depicts a schematic illustration of our JJ device structure with two sets of four-terminal Ti/Au bottom electrodes contact on each NbSe$_2$ flake, enabling simultaneous measurements of electrical transport on individual flakes as well as across the junction. Fig. 1b presents a typical optical micrograph of a 2H-NbSe$_2$ JJ device. To examine the device quality, we carried out cross-sectional high-angle annular dark-field (HAADF)-scanning transmission electron microscopy (STEM) measurement. Figure 1c shows HAADF-STEM image of device 1 with the top and bottom NbSe$_2$ layers having the same thickness of approximately 11 nm. Obviously, the interface is atomically smooth and flat without defects or impurities. As

shown in the atomically resolved image, Fig. 1d, both NbSe$_2$ flakes exhibit the same lattice structures with bulk NbSe$_2$ crystal with a 0.63 nm period and there is no evidence of oxidation at the interface. The distance between the two Nb atomic layers at the interface is 0.97 nm. This vdW gap leads to the decouple of the top and bottom NbSe$_2$ flakes, thereby forming a JJ[27,32].

Figure 1e shows the T-dependent resistance of device 1 (Fig. 1b–d) and device 2 (composed of a 9 nm top NbSe$_2$ layer and a 7 nm bottom NbSe$_2$ layer, see Supplementary Fig. S7b). Both devices exhibit a sharp superconducting transition. The transition temperature T_c, defined as the temperature corresponding to 50% drop in resistance, is 6.5 K (6.6 K) for device 1 (2).

Field-free JDE

We measured the voltage versus current characteristic (I–V curve) to examine the JDE. A sweeping DC current was applied in both forward and backward directions at 2 K in the absence of H. Results for devices 1 and 2 are displayed in Fig. 2a–d. The I–V curve measurement consists of two steps: the DC current first sweeps from negative to positive (n-0-p, as indicated by blue solid lines in Fig. 2a, b), then sweeps back from positive to negative (p-0-n, as indicated by blue dashed lines in Fig. 2a, b). I_c is defined as the critical current at which the the junction enters the normal state and I_r is the retrapping current returning to the superconducting state[22]. As shown in Fig. 2a, device 1 shows non-hysteretic behavior in I–V curves, i.e., $I_r = I_c$, indicating that the JJ device is in the strongly overdamped regime. Only a single superconducting transition occurs during the current sweeps. By contrast, for device 2, all the I–V curves exhibit hysteresis between forward and backward sweeps with $I_c > I_r$, as shown in Fig. 2b. Furthermore, the Stewart–McCumber parameter[21] $\beta_c \approx \left(\frac{4I_c}{\pi I_r}\right)^2$ of device 2 is calculated to be 4.15; $\beta_c > 1$ suggests that the JJ is in the underdamped region. Additionally, there is another transition at 1.84 mA above the I_c of JJ, which is attributed to the current-driven superconducting-to-normal transition of the NbSe$_2$
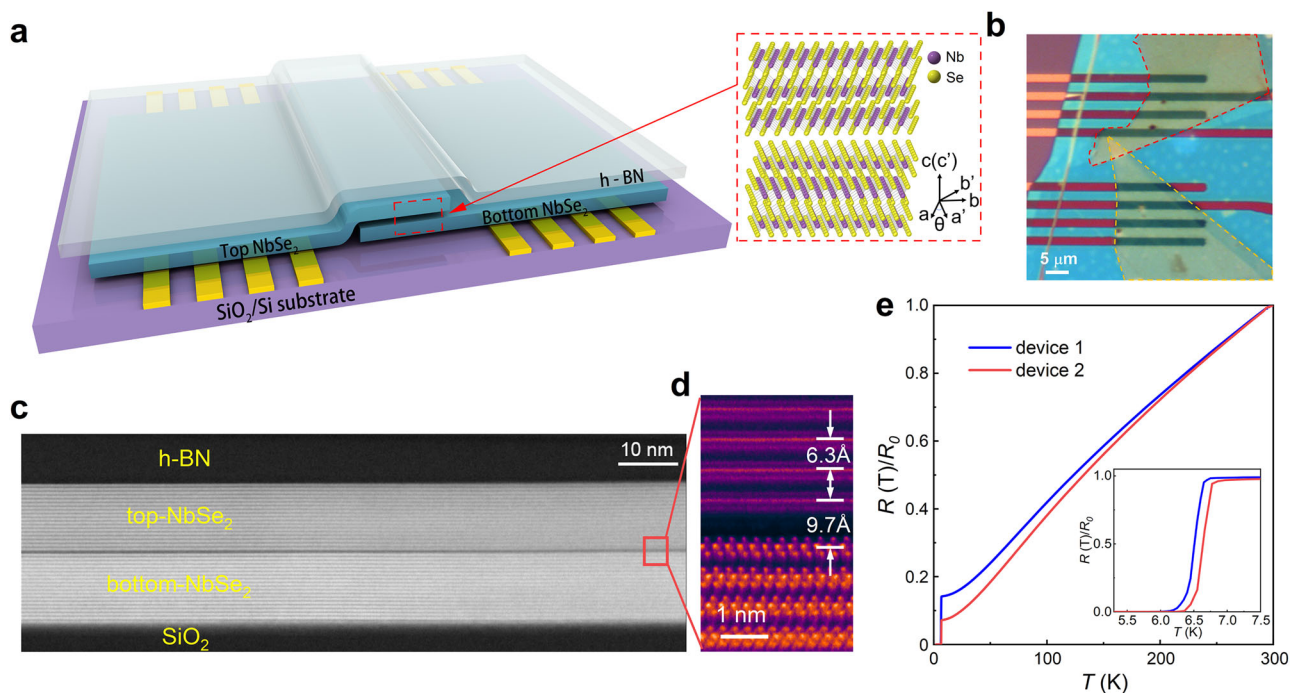

Fig. 1 | The van der Waals Josephson junction of NbSe$_2$. a The schematic of a typical NbSe$_2$ Josephson junction device, showing the h-BN protective layer, NbSe$_2$ thin flakes, Ti/Au electrodes, and SiO$_2$/Si substrate. Inset, the vertical architecture of junction, consisting of two NbSe$_2$ thin flakes. **b** Optical micrograph of device 1. Top and bottom NbSe$_2$ flakes are highlighted by red and yellow lines. **c** Cross-sectional high-angle annular dark-field (HAADF)-scanning transmission electron microscopy (STEM) image of device 1. The top and bottom NbSe$_2$ flakes have the

same thickness of around 11 nm. **d** Atomically resolved HAADF-STEM image of device 1, showing the vicinity of the interface. The distances between Nb layers in NbSe$_2$ crystals and at the interface are 0.63 and 0.97 nm, respectively. **e** Temperature dependence of resistance measured in device 1 (blue) and device 2 (red). Both devices show a sharp superconducting transition, occurring at 6.5 and 6.6 K, respectively. Inset: an expanded view of the superconducting transition.
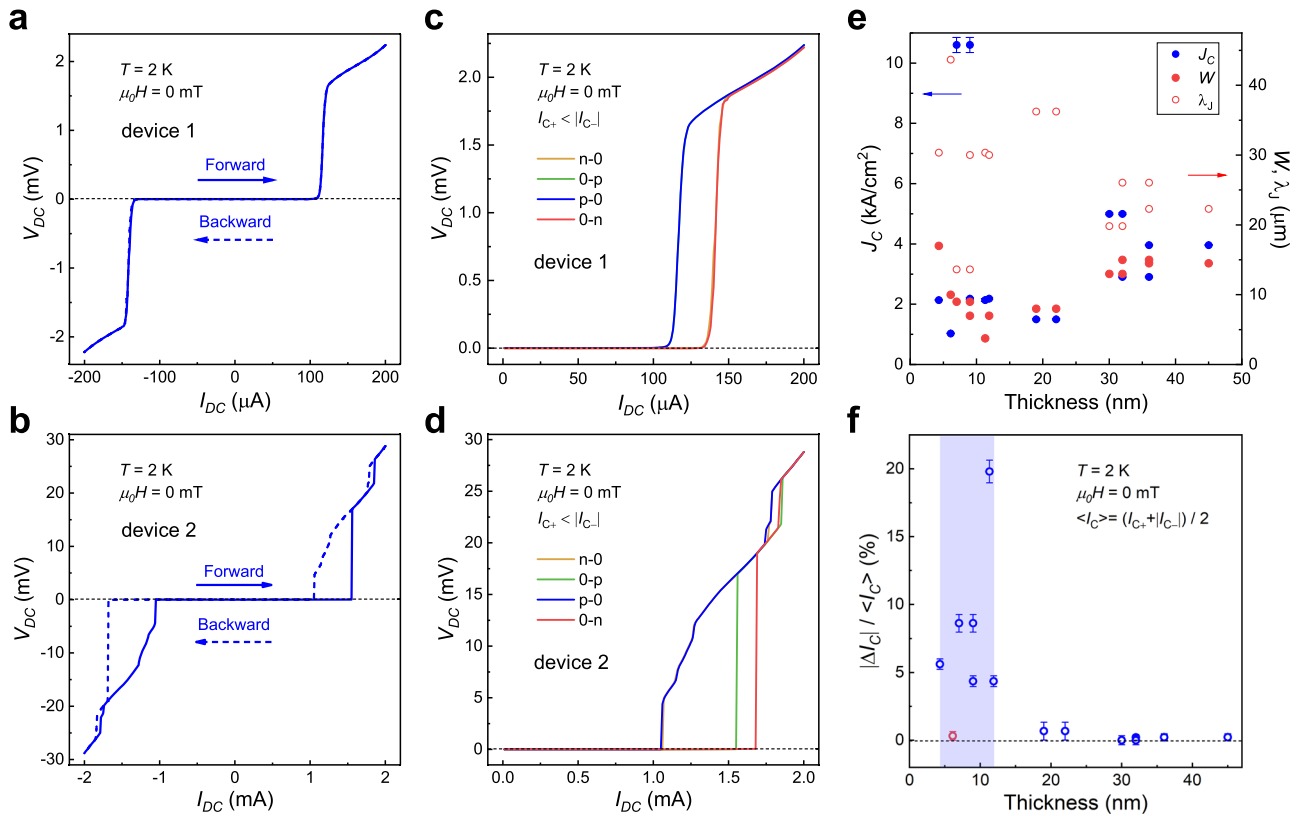
Fig. 2 | The zero-field nonreciprocal electronic transport properties. The voltage versus current characteristic (I–V curve) of device 1 (**a**) and device 2 (**b**) at 2 K and zero field. The I–V curve measurement contains two steps, i.e., forward and backward as shown by the blue solid and dashed lines, respectively. Device 1 is in the strongly overdamped regime implied by the non-hysteretic behavior in I–V curves, whereas device 2 is an underdamped Josephson junction showing a hysteretic I-V behavior. **c,d** The four branches of I–V curves: n-0, 0-p, p-0, and 0-n, denoted by orange, green, blue, and red lines, respectively. The critical supercurrents I_{c+} and $|I_{c-}|$ are different in both devices 1 and 2. **e** The supercurrent density J_c (blue dots), the junction width W (red dots), and the Josephson penetration depth λ_J (red circles) in all fabricated NbSe$_2$ vdW devices. The error bars represent the standard deviation of the critical supercurrent density values obtained from averaging multiple measurements. **f** The magnitude of zero-field Josephson diode effect (JDE) plotted against the thickness of NbSe$_2$ flakes for all devices. Blue shaded region highlights the emergence of finite zero-field JDE only in devices composed of flakes thinner than ~12 nm. The error bars are estimated from the standard deviation of the critical current values from multiple measurements.

flakes. This transition has been reported in several previous reports[11,27,33]. We point out that our devices are free of the influence of inhomogeneous current density distribution that is usually expected in a wide JJ, wherein the junction width W is larger than the Josephson penetration depth λ_J[22,28,33]. λ_J can be calculated as $\lambda_J = \sqrt{\frac{\hbar}{2\mu_0 e \Lambda J_c}}$ ($\hbar$ is the reduced Planck's constant, μ_0 is the vacuum permeability, e is the electron charge, Λ is the effective junction length and equals to $2\lambda + d$, λ is the London penetration depth of NbSe$_2$, d is the thickness of barrier, and J_c is the supercurrent density). We summarized the values of J_c, W, and λ_J of all the fabricated NbSe$_2$/NbSe$_2$ junctions in Fig. 2e. λ_J is determined to be larger than the JJ's size in devices, demonstrating that our devices are still in the narrow junction regime.

We divide the I–V curve into four branches: (i) negative to zero (n → 0), (ii) zero to positive (0 → p), (iii) positive to zero (p → 0), and (iv) zero to negative (0 → n). Subsequently, the absolute values of branches (i) and (iv) were plotted in the first quadrant together with (ii) and (iii) for a comparison, as shown in Fig. 2c,d. I_{c+} and I_{r+} are defined as the critical currents in the positive current regime (ii and iii), while I_{c-} and I_{r-} are the critical currents in the negative regime (iv and i). Due to its non-hysteretic behavior, device 1 has equal I_c and I_r in the same sweep direction ($I_{c+} = I_{r+}$, $I_{c-} = I_{r-}$). However, these currents are asymmetric with regard to the zero point. As shown in Fig. 2c, I_{c+} and $|I_{c-}|$ are evidently different. The ΔI_c of device 1 is ~−22 μA at zero field. For device 2, I_{c+} does not equal to $|I_{c-}|$ either, with a ΔI_c of −130 μA. There is a very small difference between I_{r+} and $|I_{r-}|$ with a ΔI_r of only 10 μA, considering their absolute values. These characteristics confirm the presence of a field-free JDE in both devices 1 and 2.

The discovery of JDE in NbSe$_2$/NbSe$_2$ vdW JJs without the application of H or introduction of special tunneling barriers is highly unusual. Such effect has been overlooked in all the previous works[11,27,34,35]. In these works, the thickness of the studied NbSe$_2$ flakes is typically above 20 nm, i.e., the flakes are thicker than those in devices 1 and 2 mentioned above. We confirmed that the zero-field JDE is always absent in our devices fabricated using the same technique but comprising thicker flakes (30–45 nm, Supplementary Fig. S8); on the other hand, the thick-flake-based JJs exhibit diode effect under H (Supplementary Fig. S9). These behaviors are in agreement with the existing results[7,11]. In Fig. 2f, the magnitude of zero-field JDE, defined to be the ratio $\frac{\Delta I_c}{<I_c>}$, where $<I_c> = \frac{I_{c+}+|I_{c-}|}{2}$ is the average of positive and negative critical currents, are plotted against the NbSe$_2$ flake thickness in all devices. It can be immediately figured out that zero-field JDE unambiguously emerges only in devices composed of NbSe$_2$ flakes thinner than 12 nm; this suggests the existence of a threshold thickness of approximately 12 nm for the realization of zero-field JDE (with the only exception of device 6 represented by the red symbol in Fig. 2f, which consists of two 6 nm flakes but is characterized by the absence of zero-field JDE). The fact that the occurrence of zero-field JDE is associated with reduced flake thickness demonstrates the intrinsic nature of such phenomenon in the thin-flake-based devices, i.e., it cannot be a spurious effect introduced by defective experimental setups. We further verified this point by measuring the JDE using different designs of electric circuit configurations; the outcomes are fully consistent (see Fig. S3 of Supplementary Note 2), precluding the possibility that the zero-field JDE is due to artifacts in circuits. Moreover, we also determined that the observation is not caused by trapped vortices or
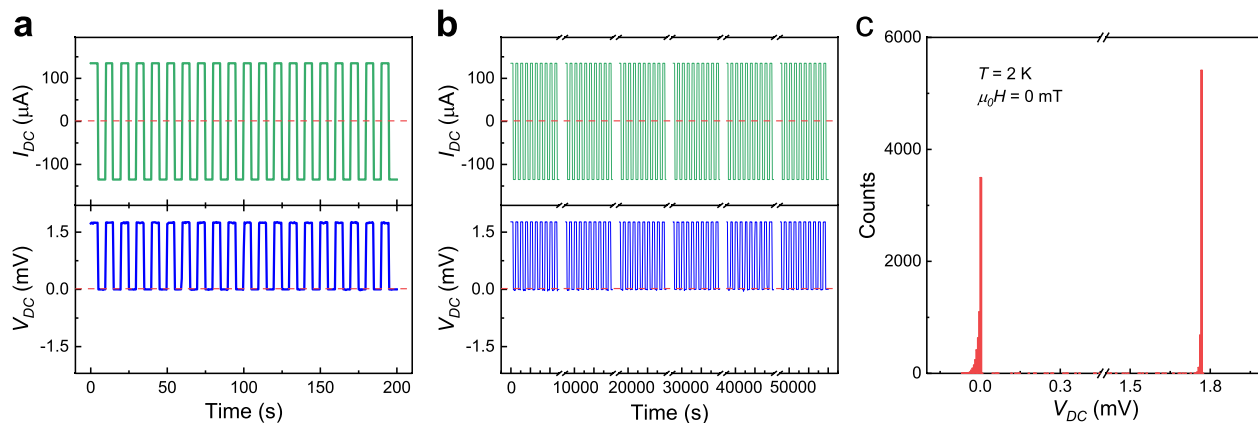
Fig. 3 | The half-wave rectification of device 1 at 2 K and zero field. a Half-wave rectification of Josephson diode effect (JDE). The green line in the top panel shows a square-wave current with an amplitude of 132 μA and a frequency of 0.1 Hz which is applied to device 1, and the blue line in the bottom panel is the voltage measured across the junction. The red dashed lines indicate the zero value. The voltage is approximately zero within the experimental resolution under the application of negative currents, yet develops a finite value when the current is switched to positive. **b** The durability test of JDE. The same square-wave current with **a** is applied more than 50,000 s consisting of 5000 continuous cycles, plotted with green line and the blue line is the junction voltage, showing no degradation of JDE. **c** Histograms of the measured voltage data in the 5000 continuous cycles of **b**.

residual flux which smear the real zero point of H. The details and results are available in Supplementary Notes 2 and 3.

The difference between I_{c+} and $|I_{c-}|$ and the sharp superconducting transition in I–V curve mean that if a current between I_{c+} and $|I_{c-}|$ is applied to the device, the JJ will be a superconductor with zero resistance for current along one direction but a normal metal with a finite resistance for the opposite direction. Therefore, we can demonstrate a rapid and clear half-wave rectification effect for a square-wave excitation. For device 1, I_{c+} = 116 μA, $|I_{c-}|$ = 138 μA, a square-wave excitation with an amplitude of 132 μA (between I_{c+} and $|I_{c-}|$) and a frequency of 0.1 Hz was applied. As illustrated in Fig. 3a, when the current is positive, a voltage of 1.75 mV can be measured, indicative of the JJ device in normal state with finite resistance. Upon the current switching to negative, the junction voltage dropped below 10^{-5} V, indicating the superconducting state of the JJ device. Furthermore, we applied the square-wave excitation current more than 50,000 s consisting of 5000 continuous cycles at 2 K without H. As shown in Fig. 3b, the junction voltage maintained consistent periodicity and can switch between high (1.75 mV) and low (near to 0) states sharply and stably throughout all cycles. Figure 3c presents the histograms of the measured junction voltages over 5000 cycles. The data are concentrated closely around the high and low voltage values, which suggests a high degree of durability and robustness in the half-wave rectification of the JJ device. The realization of stable rectification effect in absence of an external magnetic field or specific tunneling barrier can provide a promising avenue for application. It is noteworthy that this device represents the rare field-free overdamped JDE with robust superconducting rectification and high rectification ratio. The overdamped JJ has more advantages for the application of quantum devices, attributable to its single-valued I–V curve and the ultrahigh operation frequency up to THz[36,37].

Temperature dependence of JDE

The zero-field JDE was further studied by measuring I–V curves between 2 and 6 K at zero field. The DC current with a small AC excitation was swept in two steps, the same as the process mentioned above and we were able to measure the differential resistance (dV/dI) of the JJ simultaneously. As shown in Fig. 4a, there is no hysteretic behavior in the I–V curves of device 1 at all temperature, indicating that the JJ is in the overdamped regime.

We plot the temperature dependence of critical currents in two directions in Fig. 4b, and the critical currents determined from the I–V curve are identical with whose from dV/dI, as shown in Fig. 4c. The single peak in dV/dI curve confirms that there is only one superconducting transition. Both I_{c+} and $|I_{c-}|$ exhibit a monotonic increase as the temperature

decreasing. The nonreciprocity of critical currents appears simultaneously with the superconducting transition. The inset in Fig. 4b shows the non-monotonic behavior of the $|\Delta I_c|$, as a function of temperature. Initially, the $|\Delta I_c|$ increases as temperature decreasing until 4.6 K, and then $|\Delta I_c|$ decreases. Below 3.2 K, $|\Delta I_c|$ increases again and reaches its maximum value at 2 K.

To further determine the temperature dependence of the superconducting state of the JJ, we calculated the critical currents using Ambegaokar–Baratoff (AB) theory[38]:

$$\frac{I_c(T)}{I_c(0)} = \frac{\Delta(T)}{\Delta(0)} \tanh\left[\frac{\Delta(T)}{2k_B T}\right], \tag{1}$$

where Δ is the superconducting gap and k_B is the Boltzmann constant. The numerical fit curve is plotted as the black dashed line alongside the $|I_{c-}|$ data (blue circles). As shown in Fig. 4d, the $|I_{c-}|$ data fits well with AB theory and the superconducting gap at 0 K was determined as a fitting parameter, $\Delta(0)$ = 0.868 meV. The differential conductance, dI/dV, as a function of bias voltage, can be obtained from the I–V curve data. As shown in Supplementary Fig. S10, the peaks of differential conductance emerge at the value twice of superconducting gap, attributable to the tunneling of Cooper pairs[27]. The gap from differential conductance can be fitted with Bardeen–Cooper–Schrieffer (BCS) theory:

$$\Delta(T) = \Delta(0) \tanh\left(2.2\sqrt{\frac{T_c - T}{T}}\right), \tag{2}$$

where $\Delta(0)$ is the superconducting gap at 0 K and T_c is the critical temperature of the superconductivity. As shown in Fig. 4e, the experimental data is well described by the BCS theory and $\Delta(0)$ is obtained as 0.958 meV, which shows good agreement with the value from the fitting of $|I_{c-}|$ and is very close to the superconducting gap of NbSe$_2$ flakes ($\approx$1 meV)[39], indicating no degradation of superconductivity in the JJ.

Magnetic field dependence of JDE

In our studies of H-dependent critical currents, an in-plane H was applied perpendicular to the tunneling current on the JJ device (as illustrated in the inset of Fig. 5b). Figure 5a displays the color map of differential resistance as a function of the in-plane H; the critical current defined by the differential resistance (bright curve) exhibits an unusual oscillatory behavior, manifesting a deformed Fraunhofer pattern. Considering the high interface
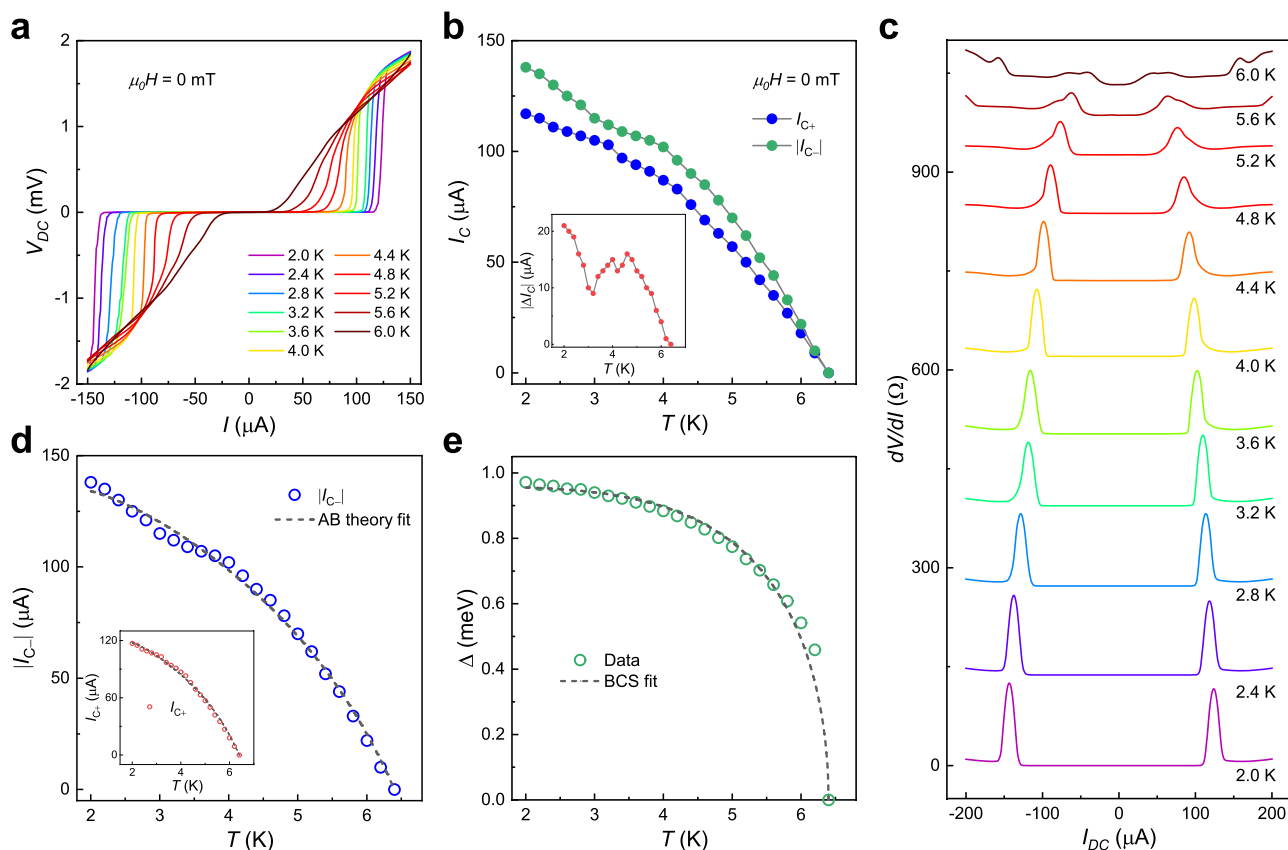
Fig. 4 | Temperature dependence of the Josephson diode effect (JDE). a The voltage versus current characteristic (I–V curve) measured on device 1 for temperature from 2 to 6 K at zero field. All the curves show non-hysteretic and asymmetric behaviors. **b** Temperature dependence of critical currents on the opposite directions. The critical supercurrents I_{c+} and $|I_{c-}|$ are represented by blue and green dots, respectively. Both critical currents increase monotonically with temperature decreasing. Inset, the non-monotonic temperature dependence of nonreciprocal component of critical currents $|\Delta I_c|$. **c** The differential resistance dV/dI as a function of current I at different temperatures. Only a single pair of peaks can be seen and the positions of peaks shift toward zero upon warming. **d** The $|I_{c-}|$ as a function of temperature for device 1. The black dashed line denotes the numerical fit using AB theory (Equation 1 in the subsection "Temperature dependence of JDE" of results). Inset is the same fit for I_{c+}. **e** The temperature dependence of superconducting gap obtained from the differential conductance curves; data show good agreement with the fitting curve based on BCS theory (dashed line, Equation 2 in the subsection "Temperature dependence of JDE" of results).

quality of our device evidenced by HAADF-STEM results (Fig. 1c,d), the non-ideal Fraunhofer pattern is likely to be associated with extrinsic effects. It is known that the Fraunhofer oscillation pattern can be influenced by many factors, including the self-field effect of supercurrent[33], the orientation of in-plane H[34] and magnetic vortices in the superconducting electrodes[11,40]. In particular, the widely observed irregular Fraunhofer pattern in vdW junctions can be attributed to the inhomogeneous widths of the device along the direction of H, which naturally explains our data[34]. Despite these, an oscillation period of 42.1 mT was observed; considering the fundamental form of Fraunhofer pattern[22]:

$$\frac{I_c(H)}{I_c(0)} = \left| \frac{\sin\left(\pi\Phi/\Phi_0\right)}{\pi\Phi/\Phi_0} \right|, \tag{3}$$

where $\Phi = (2\lambda + d)WH$, λ is the London penetration depth of NbSe$_2$, d is the thickness of barrier, W is the width of JJ, and Φ_0 is the magnetic flux quantum. For device 1, d is 0.34 nm as determined by HAADF-STEM result in Fig. 1d and W is 3.75 μm, we can figure out that λ is 6.5 nm, which is in agreement with previously reported values for NbSe$_2$ in JJs[11,27]. Simultaneously, we measured the temperature dependence of the upper critical field for in-plane H of the NbSe$_2$ flake in device 1. It significantly exceeded the Pauli limit and an anomalous upturn was observed, as shown in Supplementary Fig. S11, suggesting the existence of an orbital FFLO state above a threshold in-plane H[29]; the FFLO state may have an influence on the

field-induced SDE/JDE[10] in the NbSe$_2$ flakes[7], but is unlikely to contribute to the zero-field JDE reported herein.

Figure 5b displays ΔI_c of device 1 plotted as a function of H. In this device, ΔI_c is negative (i.e., $I_{c+} < |I_{c-}|$) at low fields (see Fig. 2c). As the in-plane field is ramped up, ΔI_c approaches zero, and a sign reversal of ΔI_c occurs at around 32 mT. At higher fields ΔI_c remains positive with $I_{c+} > |I_{c-}|$, as shown in Fig. 5c. Such field dependence is independent of the field sweep direction. Figure 5d displays the I–V curve measured at −40 mT, where the I_{c+} also exceeds $|I_{c-}|$, similar to the I–V curve taken at +40 mT (Fig. 5c). For device 2 that also exhibits zero-field JDE (Fig. 2d) and half-wave rectification (Supplementary Fig. S12), ΔI_c is consistently symmetric in H (yet without the sign reversal, Supplementary Fig. S12b). In contrast, JJs composed of thicker NbSe$_2$ flakes (devices 3, 4, and 5) in which the zero-field nonreciprocal transport is absent are characterized by a centrosymmetric $\Delta I_c(H)$ profile (Supplementary Figs. S8 and S9). This field-induced diode effect, which is antisymmetric in H, has been widely reported in many superconducting devices[4,7,10]. The distinct field evolutions strongly imply different physical origins of field-free and field-induced JDE in these JJs. According to existing understandings, the field-induced JDE has several possible origins (such as magnetochiral anisotropy, finite momentum Cooper pairing, or spin–orbit interaction); since the TRSB results from H, the sign of JDE thus depends on the polarity of H. Conversely, the field-free JDE in our devices do not rely on the field-induced TRSB and is thus irrelevant of the polarity of H. The symmetric field suppression of this effect
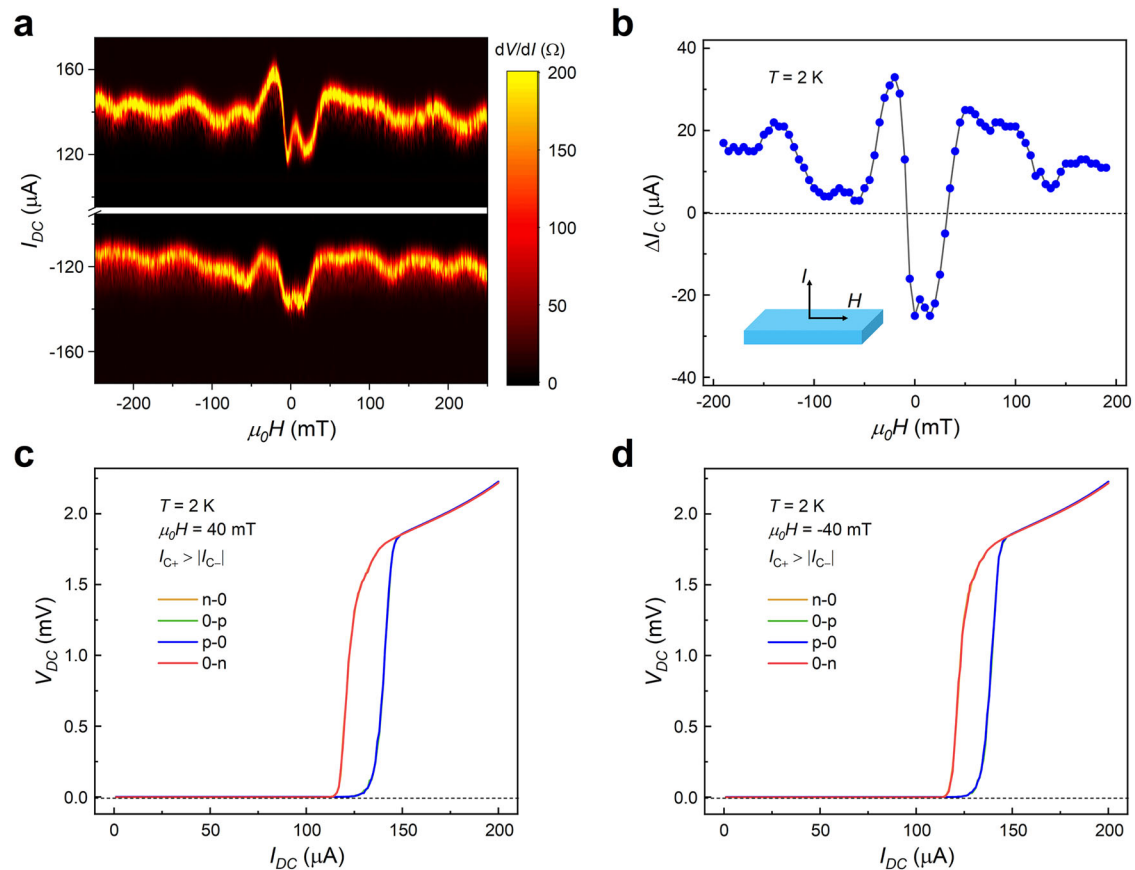
Fig. 5 | Magnetic field dependence of the Josephson diode effect (JDE). a Color map of differential resistance (dV/dI) as a function of in-plane magnetic field and current at 2 K, showing a non-ideal Fraunhofer pattern with an oscillation period of 42.1 mT. Additional features are observed around zero field. **b** The nonreciprocal component of critical currents ΔI_c versus the in-plane field, showing a roughly symmetric field dependence with a sign reversal occurring for both negative and positive fields. Inset is a schematic of the experimental setup. **c,d** The absolute value of the voltage versus current characteristic (I–V curve) at $\mu_0 H = 40$ mT and -40 mT, respectively. For both fields, the non-reciprocal behavior is observed but with critical supercurrents I_{c+} larger than $|I_{c-}|$, which is contrary to the curve at zero field.

again points toward its intrinsic nature, speaking against the trivial origins, such as residual flux or trapped vortex (Supplementary Note 3).

Discussion

According to the most recent understandings for equilibrium systems, the diode effect in retrapping current, $|I_{r+}| \neq |I_{r-}|$, can be achieved in devices in which only the IS is broken (i.e., under a TR-invariant condition); in contrast, the prerequisite of observing JDE with $|I_{c+}| \neq |I_{c-}|$ is the simultaneous breaking of IS and TRS[3,16–20]. Our data of JDE (Fig. 2) clearly point to the latter case, thus the breaking of both TRS and IS is an rigorous requirement for our vdW JJ devices 1 and 2. The IS breaking is a common phenomenon in JJ devices because of their stacked structure: there are misalignment and misorientation at the vdW interface[27]; moreover, at the interface, the topmost NbSe$_2$ layers on each flakes naturally experience a top-bottom asymmetry due to the fact that the vdW gap is much larger than the interlayer spacing in the NbSe$_2$ crystals (Fig. 1d). The strain effect arising during the transfer and stacking process is an important factor affecting the electronic structures of thin flakes and can also lead to the IS breaking due to the distinct strains on the top and bottom flakes of junctions[41]. In addition, the 2H-NbSe$_2$ monolayer at the interface itself has a noncentrosymmetric crystal structure. Consequently, it is not surprising that our vdW JJs inherently break the IS.

The mechanism of the TRSB in our devices is more intricate. The zero-field JDE unambiguously corroborates spontaneous TRSB in the superconducting state, yet such an unusual symmetry-breaking effect is totally unexpected for the well-known conventional s-wave superconductor 2H-NbSe$_2$. We examined the 2H-NbSe$_2$ crystals used in experiments. They all have very high crystal quality and the magnetic impurity is negligible, as shown in Supplementary Fig. S13, excluding extrinsic magnetism as the origin of TRSB. (We also measured the I–V curve of NbSe$_2$ flake in device 1 and observed symmetric critical current at $H = 0$, as shown in Fig. S13d.) Nonetheless, the skewed and centrosymmetric features appearing in the Fraunhofer pattern (Fig. 5a) and a local minimum of I_c at a small finite field (Supplementary Fig. S14), both of which resemble the typical behaviors of magnetic JJs[14,28], point toward the realization of a nontrivial JJ with non-zero phase at zero field. Such phenomenon again provides evidence supporting the spontaneous TRSB in our 2H-NbSe$_2$ vdW JJs. Several theoretical proposals have suggested that spontaneous TRSB can occur in JJs between a multi-band superconductor and a conventional (single-gap) superconductor due to the frustration between order parameters[25,26]. Although 2H-NbSe$_2$ is an exemplary two-band superconductor[42,43], our devices are homostructures composed of two identical NbSe$_2$ flakes without apparent factors provoking the order parameter frustration between them. The applicability of these multi-band TRSB models is thus questionable. The NbSe$_2$ flakes used to fabricate our devices were exfoliated from the same crystals and the flakes in device 1 even have the same thicknesses. Therefore, the nonreciprocity in our devices is unlikely to come from the nonlinear capacitance[17]. Recent studies have reported that the nonreciprocity at $H = 0$ may alternatively stem from the TRSB effect introduced by dissipation in the presence of strong electron correlations; in such case, the diode effects are characteristics of a nonequilibrium system[41,44]. Nonetheless, this is unlikely to serve as the explanation of our observations because the electron correlation in NbSe$_2$ is believed to be rather weak.

It should be mentioned that not all our 2H-NbSe$_2$ JJs composed of thin NbSe$_2$ flakes exhibit the zero-field JDE; an exception (device 6) in which the nonreciprocal critical current is absent is shown in Supplementary Figs. S15 and S16. The distinct behaviors between devices may be indicative of TRSB mechanisms relying on the junction geometry, such as the twist angle between the top and bottom layers. Theoretical works on twisted JJs between nodal superconductors[23,24,45] point out that spontaneous TRSB can happen around specific twist angles (so-called "magic angles") and a field-free JDE can thus be established; these proposals have been recently verified in a twisted JJ composed of Bi$_2$Sr$_2$CaCu$_2$O$_{8+x}$ crystals[15]. Numerous studies have confirmed that 2H-NbSe$_2$ is an anisotropic *s*-wave superconductor with strongly *k*-dependent superconducting gap[27,39,46]. Therefore, it is worthy to test whether the twisted JJ models for nodal superconductors are valid in our devices. We examined the twist angles between two NbSe$_2$ layers using electron back-scattered diffraction (EBSD) (see Supplementary Fig. S7). The twist angles of devices 1 and 2 (both show zero-field JDE) were determined to be 21° and 25°, respectively, whilst device 6 featuring the absence of zero-field JDE has a twist angle of 26°, i.e., very close to that in device 2. Whereas orbital magnetism driven by twist angle can give rise to spontaneous TRSB and consequently field-free SDE in graphene-based devices[12,47,48], this mechanism is most likely irrelevant in our devices as suggested by the lack of characteristic hysteretic features under field sweeps (Supplementary Note 4 and Supplementary Fig. S6). Therefore all the existing evidence seems to contradict the scenario that TRSB corresponds to specific twist angles in our NbSe$_2$ JJs. The origins of TRSB as well as difference between devices are yet to be determined at this stage.

Our results nevertheless demonstrate that it is unnecessary to introduce external fields, stray fields, or exotic superconductivity to realize JDE: a zero-field JDE can even develop in a vdW JJ between two *s*-wave superconductors, without the incorporation of special tunneling barriers or ferromagnetic layers. Benefiting from their simple design, broad range for potential material choice and high device performance (as justified by the stable and robust superconducting half-wave rectification effect over 5000 continuous cycles, Fig. 3), these vdW JJs may serve as promising candidates for practical device application. On the other hand, mechanism of the spontaneous TRSB effect herein is not fully understood within the framework of any existing theories. Further theoretical explorations are urgently awaited to interpret the observed zero-field JDE in vdW JJs composed of only conventional superconductors.

Methods

Crystal growth
High-quality 2H-NbSe$_2$ single crystals used in this work were synthesized through chemical vapor transport method. Stoichiometric ratio of Nb (powder) and Se (pellet) were evacuated and sealed in a 250 mm long and 20 mm diameter quartz tube with 0.2% excess of Se and 150 mg iodine. We added a very slight excess of Se to ensure stoichiometry in crystals. Then, the tube was placed in a double zone furnace horizontally with a temperature gradient from 690 °C to 750 °C for three weeks. After that, sheet crystals of 2H-NbSe$_2$ can be found at the low-temperature end.

Device fabrication
The JJ devices were fabricated through a dry-transfer method in a top-down process which can avoid the residue of polymers. To minimize surface oxidation and decay of NbSe$_2$ layers, the entire fabrication process was carried out in an Ar-filled glovebox (H$_2$O, O$_2$ < 0.1 ppm). NbSe$_2$ and h-BN crystals were exfoliated on SiO$_2$ (285 nm)/Si substrates using Scotch tapes. Ti (3 nm)/Au (20 nm) bottom electrodes were deposited onto SiO$_2$/Si substrate using photolithography and electron beam evaporation. The h-BN thin flake, the top NbSe$_2$, and bottom NbSe$_2$ were sequentially picked up at 40 °C by a thick polydimethylsiloxane film coated with a thin layer of polypropylene carbonate (PPC), which was prepared on a glass slide[31]. The stack was then transferred onto the pre-patterned metal electrode at 90 °C and the PPC was removed in chloroform. Devices 1, 2, and 6 were fabricated with thin NbSe$_2$ flakes of around 10 nm and devices 3, 4, and 5 were fabricated with thicker flakes (more than 30 nm).

Transport measurements
Transport measurements were carried out in physical property measurement systems (Quantum Design) down to 2 K. For the measurement of *T*-dependent resistance, an AC current of 10 μA with a frequency of 19.711 Hz was applied and the voltage signal across the junction was measured using a SR830 lock-in amplifier. The DC and square-wave measurements were performed by a Keithley 6221 current source and a Keithley 2182A nanovoltmeter. For *I–V* and d*V*/d*I* (including the Fraunhofer pattern) measurements, a Keithley 6221 was used to inject DC current and a small AC excitation (10 nA and 277 Hz) was supplied by the SR830 lock-in amplifier combined with a 1 MΩ high precision resistor. The DC voltage was measured by Keithley 2182A nanovoltmeter and the AC voltage signal was amplified by the SR560 preamplifier and measured by SR830. To obtain a better signal-to-noise ratio, two sets of filters were used in the d*V*/d*I* measurement : (i) four homemade low-pass filters with cut-off frequency around 470 kHz, (ii) the built-in filter of the preamplifier SR560. More details of the measurement setups are available in Supplementary Note 1.

Structural analysis of devices
Scanning electron microscope (SEM)-EBSD experiments were performed using an Oxford Symmetry S2. For cross-sectional STEM measurement, the samples were prepared using a focused ion beam with Ga ions. Then, STEM experiments were conducted on a 300 kV Themis Z microscope. The atomic resolved HAADF-STEM images were collected with a 25 mrad convergent angle and a collection angle of 41–200 mrad.

Data availability
The data supporting the findings of this study are available from the corresponding authors upon reasonable request.

Code availability
The code used to analyze the data is available from the corresponding authors upon reasonable request.

References
1. Strambini, E. et al. Superconducting spintronic tunnel diode. *Nat. Commun.* **13**, 2431 (2022).
2. Chahid, S., Teknowijoyo, S., Mowgood, I. & Gulian, A. High-frequency diode effect in superconducting Nb$_3$Sn microbridges. *Phys. Rev. B* **107**, 054506 (2023).
3. Zhang, Y., Gu, Y., Li, P., Hu, J. & Jiang, K. General theory of Josephson diodes. *Phys. Rev. X* **12**, 041013 (2022).
4. Ando, F. et al. Observation of superconducting diode effect. *Nature* **584**, 373–376 (2020).
5. Narita, H. et al. Field-free superconducting diode effect in noncentrosymmetric superconductor/ferromagnet multilayers. *Nat. Nanotechnol.* **17**, 823–828 (2022).
6. Hou, Y. et al. Ubiquitous superconducting diode effect in superconductor thin films. *Phys. Rev. Lett.* **131**, 027001 (2023).
7. Bauriedl, L. et al. Supercurrent diode effect and magnetochiral anisotropy in few-layer NbSe$_2$. *Nat. Commun.* **13**, 4266 (2022).
8. Baumgartner, C. et al. Supercurrent rectification and magnetochiral effects in symmetric Josephson junctions. *Nat. Nanotechnol.* **17**, 39–44 (2022).
9. Jeon, K.-R. et al. Zero-field polarity-reversible Josephson supercurrent diodes enabled by a proximity-magnetized Pt barrier. *Nat. Mater.* **21**, 1008–1013 (2022).

10. Pal, B. et al. Josephson diode effect from Cooper pair momentum in a topological semimetal. *Nat. Phys.* **18**, 1228–1233 (2022).
11. Wu, H. et al. The field-free Josephson diode in a van der Waals heterostructure. *Nature* **604**, 653–656 (2022).
12. Díez-Mérida, J. et al. Symmetry-broken Josephson junctions and superconducting diodes in magic-angle twisted bilayer graphene. *Nat. Commun.* **14**, 2396 (2023).
13. Anwar, M. S. et al. Spontaneous superconducting diode effect in non-magnetic Nb/Ru/Sr$_2$RuO$_4$ topological junctions. *Commun. Phys.* **6**, 290 (2023).
14. Qiu, G. et al. Emergent ferromagnetism with superconductivity in Fe(Te,Se) van der Waals Josephson junctions. *Nat. Commun.* **14**, 6691 (2023).
15. Zhao, S. Y. F. et al. Time-reversal symmetry breaking superconductivity between twisted cuprate superconductors. *Science* **382**, 1422–1427 (2023).
16. Steiner, J. F., Melischek, L., Trahms, M., Franke, K. J. & von Oppen, F. Diode effects in current-biased Josephson junctions. *Phys. Rev. Lett.* **130**, 177002 (2023).
17. Misaki, K. & Nagaosa, N. Theory of the nonreciprocal Josephson effect. *Phys. Rev. B* **103**, 245302 (2021).
18. Daido, A., Ikeda, Y. & Yanase, Y. Intrinsic superconducting diode effect. *Phys. Rev. Lett.* **128**, 037001 (2022).
19. He, J. J., Tanaka, Y. & Nagaosa, N. A phenomenological theory of superconductor diodes. *N. J. Phys.* **24**, 053014 (2022).
20. Ilić, S. & Bergeret, F. S. Theory of the supercurrent diode effect in Rashba superconductors with arbitrary disorder. *Phys. Rev. Lett.* **128**, 177001 (2022).
21. Likharev, K. K. Superconducting weak links. *Rev. Mod. Phys.* **51**, 101–159 (1979).
22. Tinkham, M. *Introduction to Superconductivity* (Dover Pub. Inc., 1996).
23. Can, O. et al. High-temperature topological superconductivity in twisted double-layer copper oxides. *Nat. Phys.* **17**, 519–524 (2021).
24. Volkov, P. A. et al. Josephson diode effects in twisted nodal superconductors. *Phys. Rev. B* **109**, 094518 (2024).
25. Ng, T. K. & Nagaosa, N. Broken time-reversal symmetry in Josephson junction involving two-band superconductors. *Europhys. Lett.* **87**, 17003 (2009).
26. Avishai, Y. & Ng, T. K. Broken time-reversal symmetry in a Josephson junction with an Anderson impurity between a two-band and a single-band superconductor. *Phys. Rev. B* **81**, 104501 (2010).
27. Yabuki, N. et al. Supercurrent in van der Waals Josephson junction. *Nat. Commun.* **7**, 10616 (2016).
28. Ai, L. et al. Van der Waals ferromagnetic Josephson junctions. *Nat. Commun.* **12**, 6580 (2021).
29. Wan, P. et al. Orbital Fulde-Ferrell-Larkin-Ovchinnikov state in an Ising superconductor. *Nature* **619**, 46–51 (2023).
30. Xi, X. et al. Ising pairing in superconducting NbSe2 atomic layers. *Nat. Phys.* **12**, 139–143 (2016).
31. Wang, L. et al. One-dimensional electrical contact to a two-dimensional material. *Science* **342**, 614–617 (2013).
32. Liu, K. et al. Evolution of interlayer coupling in twisted molybdenum disulfide bilayers. *Nat. Commun.* **5**, 4966 (2014).
33. Kim, M. et al. Strong proximity Josephson coupling in vertically stacked NbSe$_2$-Graphene-NbSe$_2$ van der Waals junctions. *Nano Lett.* **17**, 6125–6130 (2017).
34. Chen, X., Poortvliet, M., van der Molen, S. J. & de Dood, M. J. A. Interface shape dependent interference patterns of NbSe$_2$ heterostructure Josephson junctions. *Phys. Rev. B* **107**, 094522 (2023).
35. Farrar, L. S. et al. Superconducting quantum interference in twisted van der Waals heterostructures. *Nano Lett.* **21**, 6725–6731 (2021).
36. Likharev, K. K. & Semenov, V. K. RSFQ logic/memory family: a new Josephson-junction technology for sub-terahertz-clock-frequency digital systems. *IEEE Trans. Appl. Superconduct.* **1**, 3–28 (1991).
37. Kleiner, R., Koelle, D., Ludwig, F. & Clarke, J. Superconducting quantum interference devices: state of the art and applications. *Proc. IEEE* **92**, 1534–1548 (2004).
38. Barone, A. & Paterno, G. *Physics and Applications of the Josephson effect* (Wiley, 1982).
39. Khestanova, E. et al. Unusual suppression of the superconducting energy gap and critical temperature in atomically thin NbSe$_2$. *Nano Lett.* **18**, 2623–2629 (2018).
40. Golod, T. & Krasnov, V. M. Demonstration of a superconducting diode-with-memory, operational at zero magnetic field with switchable nonreciprocity. *Nat. Commun.* **13**, 3658 (2022).
41. Liu, F. et al. Superconducting diode effect under time-reversal symmetry. *Sci. Adv.* **10**, eado1502 (2024).
42. Yokoya, T. et al. Fermi surface sheet-dependent superconductivity in 2H-NbSe$_2$. *Science* **294**, 2518–2520 (2001).
43. Huang, C. L. et al. Experimental evidence for a two-gap structure of superconducting NbSe$_2$: a specific-heat study in external magnetic fields. *Phys. Rev. B* **76**, 212504 (2007).
44. Morimoto, T. & Nagaosa, N. Nonreciprocal current from electron interactions in noncentrosymmetric crystals: roles of time reversal symmetry and dissipation. *Sci. Rep.* **8**, 2973 (2018).
45. Tummuru, T., Plugge, S. & Franz, M. Josephson effects in twisted cuprate bilayers. *Phys. Rev. B* **105**, 064501 (2022).
46. Cho, C.-W. et al. Nodal and nematic superconducting phases in NbSe$_2$ monolayers from competing superconducting channels. *Phys. Rev. Lett.* **129**, 087002 (2022).
47. Kuiri, M. et al. Spontaneous time-reversal symmetry breaking in twisted double bilayer graphene. *Nat. Commun.* **13**, 6468 (2022).
48. Lin, J.-X. et al. Zero-field superconducting diode effect in small-twist-angle trilayer graphene. *Nat. Phys.* **18**, 1221–1227 (2022).

Acknowledgements

Author contributions
J.M., Z.X., and X.-H.C. conceived and designed the experiments. J.M. grew the single crystals. J.M. fabricated the devices with help from W.Z., B.L., W.W., and X.-Y.C. J.M. performed transport measurements. H.W., Z.W., and J.T. performed STEM measurements and relevant data analysis. S.W., H.W., and B.G. performed EBSD measurements. J.M., Z.-Y.W., K.J., Z.X., and X.-H.C. performed the data analysis. J.M. and Z.X. wrote the manuscript with inputs from K.J. and X.-H.C. All authors discussed the results and commented on the manuscript.

Competing interests
The authors declare no competing interests.

Additional information

Supplementary information The online version contains supplementary material available at https://doi.org/10.1038/s42005-025-02054-9.

Correspondence and requests for materials should be addressed to Ziji Xiang or Xian-Hui Chen.

Peer review information *Communications Physics* thanks the anonymous reviewers for their contribution to the peer review of this work. [A peer review file is available].

Reprints and permissions information is available at http://www.nature.com/reprints

Publisher's note Springer Nature remains neutral with regard to jurisdictional claims in published maps and institutional affiliations.